Available online at www.sciencedirect.com
ScienceDirect
Trans. Nonferrous Met. Soc. China 32(2022) 3276−3290
Transactions of Nonferrous Metals Society of China
www.tnmsc.cn

# Formation mechanism of basin-like depression defect in electric upsetting process of Ni80A superalloy

Guo-zheng QUAN[1,2,3], Xue SHENG[1], Kun YANG[1], Yan-ze YU[1], Wei XIONG[4]

1. Chongqing Key Laboratory of Advanced Mold Intelligent Manufacturing, College of Materials Science and Engineering, Chongqing University, Chongqing 400044, China;
2. State Key Laboratory of Materials Processing and Die & Mould Technology, Huazhong University of Science and Technology, Wuhan 430074, China;
3. Nanjing Jiepin Intelligent Technology Co., Ltd., Nanjing 210000, China;
4. Key Laboratory of Advanced Reactor Engineering and Safety of Ministry of Education, Collaborative Innovation Center of Advanced Nuclear Energy Technology, Institute of Nuclear and New Energy Technology, Tsinghua University, Beijing 100084, China

Received 3 September 2021; accepted 31 December 2021

**Abstract:** A kind of surface instability, basin-like depression defect companied by mixed grain structure at the bottom of large-scale valve during electric upsetting process, would significantly influence the microstructures and mechanical properties of components. In order to analyze the forming process of the basin-like depression defect, a finite element model for the electric upsetting process of Ni80A superalloy was developed using multi-field and multi-scale coupling analysis method. Subsequently, a series of parameters loading path schemes for force and current were designed by varying the initial value, peak value and value level, and their effects on basin-like depression and mixed grain structure were simulated and uncovered. It is concluded that the changes of heating speed and pressurization speed result in the different flow velocities between the inner and outer layers of billet, thus exerting the basin-like depression. Simulation results also indicate that these defects can be optimized through the parameter coordination between force and current. Finally, the validity and reliability of the finite element model were verified by physical experiments in electric upsetting process.

**Key words:** electric upsetting process; defect; Ni80A superalloy; microstructure evolution; mixed grain structure

## 1 Introduction

Large-scale valve is a kind of typical disc-rod component that works as the mostly stressed exhaust controller in a working cycle of two-stroke diesel engine. Its severe serving conditions involving high temperature, high pressure, high corrosion, high scouring velocity, etc, make itself a vulnerable component in the whole engine. Consequently, its excellent mechanical properties and even its excellent serving performance are pursued [1−3]. Ni-based heat-resistant superalloys are always extensively applied in two-stroke engine valves, meanwhile, hot forging is considered as an efficient approach to achieve the pursued mechanical properties. However, the material flowing and the microstructure evolution in a hot forging process of this type alloy exhibit very high sensitivity to the processing parameters including temperature, strain and strain rate [4−6].

As a kind of typical disc-rod component having a very large difference in diameter between the original bar and the disc, large-scale valves

**Corresponding author:** Guo-zheng QUAN, Tel: +86-15922900904, Fax: +86-23-65111493, E-mail: quangz3000@sina.com
DOI: 10.1016/S1003-6326(22)66019-9

always rely on the electrical upsetting process. In such a process as shown in Fig. 1, a direct current with step change is passed into a portion of the bar material, meanwhile, the hydraulic force is loaded on another end of the bar. Thus, on the one hand, the portion loaded by current is heated up to the plastic state by the electrical resistance of material itself; on the other hand, the hot material is yielded and compressed by the force. As this process is continued, a large portion of the bar material will be formed into a desirable shape. For a long-time electrical upsetting process, a kind of surface instability defect, i.e. basin-like depression always appears at the disc bottom of the formed piece. It is certain that the three basic process parameters including strain, strain rate and temperature determine a hot forming process. For an electrical upsetting process, these three parameters are induced by the two key variables including current and upsetting force. Consequently, the loading mode design and optimization of the two process variables are so significant.

The surface instability defect, basin-like depression, always induces the microstructural issue of mixed grains. As shown in Fig. 2, a region of mixed grains extends from one corner of the basin-like depression. During a hot forming process the occurrence of mixed grains is determined by the comprehension of grain growth mechanism and dynamic recrystallization (DRX) mechanism which are sensitive to the three basic process parameters including strain, strain rate and temperature. Near the basin-like depression the region of mixed grains is a typical consequence of the uneven distribution of these three process parameters [7−9]. The existence of mixed grain defect always results in the decline of comprehensive properties related to grain boundary and mechanical properties of a component. Therefore, it is significant to study the forming mechanisms of the basin-like depression defect in an electric upsetting process. It is generally recognized that grain size difference in mixed grain domain exceeds two grades in a field of microscopic view [10]. To identify the mixed grain domain, two grades in grain size at basin-like depression domain correspond to grain size difference of approximately 40 μm. So, in simulation diagram of grain size, one interval in legend label is set as about 20 μm. At local domain of simulation results, in Fig. 2(c), the number of intervals in legend label is more than 2. Such a domain is considered as mixed grain structure.

So far, previous researchers have proposed the influence of processing parameters on electric upsetting. NUASRI and AUE-U-LAN [11] evaluated anvil speed, upsetting load and heating voltage on the material flow as well as the heating characteristics in electric upsetting process. JEONG et al [12] researched the influence of electric current and the upset load on valve forming process and its shape optimization. ELAIYARAJA and PERIYASAMY [13] acquired different shapes of workpieces without defects by varying upset pressure, anvil position and anvil velocity of electric upsetting process. For the specific defect investigation, SUN et al [14] studied the damage in microstructure of deformed material which is induced by the overheat effect during electric

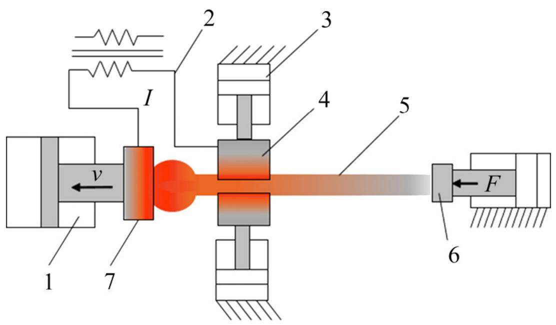


**Fig. 1** Schematic drawing of electric upsetting process: 1−Anvil cylinder; 2−Secondary transformer; 3−Clamping cylinder; 4−Clamping electrode; 5−Workpiece; 6−Upsetting cylinder; 7−Anvil

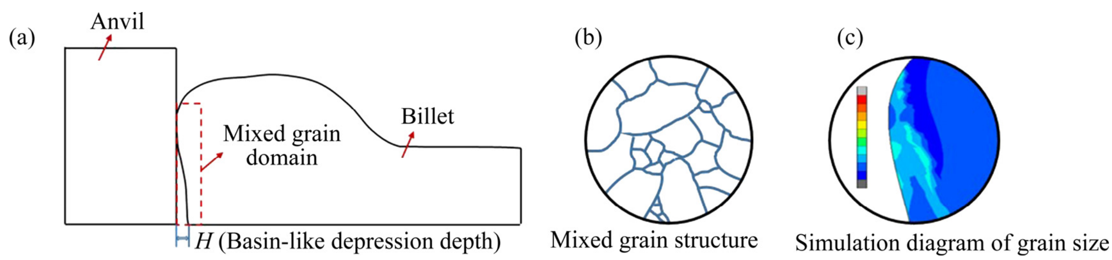


**Fig. 2** Schematic drawing of basin-like depression (a), mixed grain structure (b), and simulation result of grain size (c)

upsetting process. QUAN et al [15] reported that the change of material resistivity would lead to secondary upsetting defect of electric upsetting. NUASRI and AUE-U-LAN [16] also paid attention to the influence of the different size chamfers on defect of "surface dimple" in electric upsetting process. In addition to macro analysis on shape, QUAN et al [17] constructed a finite element (FE) model with electrical–thermal–mechanical multi-field coupling and macro–micro multi-scale coupling methods to reveal the microstructural evolution in electric upsetting process for 3Cr20Ni10W2 alloy, which provides a basis for the subsequent microscopic investigations. Several such investigations reveal that the electric upsetting parameters are related to the forming shape and grain uniformity. However, few investigations of the basin-like depression and the mixed grain structure defects in the electric upsetting process have been carried out.

In the present work, in allusion to the defect of basin-like depression commonly existed in large scale electric upsetting, multi-field and multi-scale coupling electric upsetting model was constructed by the thought of simplified models. The finite element simulation of electric upsetting for Ni80A superalloy was carried out, and the forming process of the defect was analyzed. The investigation of defects based on different currents and forces was redesigned, from which the influence of the two key variables on basin-like depression and mixed grain structure was uncovered. Simulation results indicate that the defect mitigation through parameter optimization is feasible.

## 2 Finite element model of electric upsetting process

### 2.1 Multi-field and multi-scale coupling analysis method

The numerical analysis of the electric upsetting process as a coupled issue involving electric, thermal and mechanical field, and the microstructure evolution induced by the comprehension of two mechanisms including grain growth and DRX, can be summarized as two solutions, i.e., electrical–thermal–mechanical multi-field coupling and macro–micro multi-scale coupling.

The usual finite element solvers utilizing the staggered solution procedure, can solve the multi-field coupling issue. In this approach, nodal voltage, nodal temperature and nodal displacement are achieved by solving electric, thermal, and mechanical problem, respectively. The solution matrixes concerning electric, thermal and mechanical methods are expressed as [18]

$$\begin{cases} \boldsymbol{K}^{\mathrm{E}}(\boldsymbol{T})\boldsymbol{V}=\boldsymbol{I} \\ \boldsymbol{C}^{\mathrm{T}}(\boldsymbol{T})\dot{\boldsymbol{T}}+\boldsymbol{K}^{\mathrm{T}}(\boldsymbol{T})\boldsymbol{T}=\boldsymbol{Q}+\boldsymbol{Q}^{\mathrm{E}}+\boldsymbol{Q}^{\mathrm{I}}+\boldsymbol{Q}^{\mathrm{F}} \\ \boldsymbol{M}\ddot{\boldsymbol{u}}+\boldsymbol{D}\ddot{\boldsymbol{u}}+\boldsymbol{K}^{\mathrm{M}}(\boldsymbol{T},\ \boldsymbol{u},\ \boldsymbol{t})\boldsymbol{u}=\boldsymbol{F}+\boldsymbol{F}^{\mathrm{T}} \end{cases} \tag{1}$$

where $\boldsymbol{V}$, $\boldsymbol{T}$, $\boldsymbol{u}$ and $\boldsymbol{I}$ are the node voltage vector, the node temperature vector, the node displacement vector, and the node current vector, respectively; $\boldsymbol{K}^{\mathrm{E}}(\boldsymbol{T})$, $\boldsymbol{C}^{\mathrm{T}}(\boldsymbol{T})$, and $\boldsymbol{K}^{\mathrm{T}}(\boldsymbol{T})$ are the potential matrix, the heat capacity matrix, and the thermal conductivity matrix, respectively, which are related to the temperature; $\boldsymbol{Q}$ is the flux vector; $\boldsymbol{Q}^{\mathrm{E}}$ is the heat generated due to the electrical flow vector; $\boldsymbol{Q}^{\mathrm{I}}$ is the heat generated due to the plastic deformation vector; $\boldsymbol{Q}^{\mathrm{F}}$ is the heat generation due to the friction vector; $\boldsymbol{M}$ is the mass matrix; $\boldsymbol{D}$ is the damping matrix; $\boldsymbol{K}^{\mathrm{M}}(\boldsymbol{T}, \boldsymbol{u}, \boldsymbol{t})$ is the stiffness matrix associated with temperature, strain and time; $\boldsymbol{F}$ is the vector of the external applied force; $\boldsymbol{F}^{\mathrm{T}}$ is a vector of forces generated by the thermal strain.

Figure 3 illustrates the schematic diagram of coupling relationships about electrical–thermal–mechanical multi-fields [18]. During the coupling process, heat generation $\boldsymbol{Q}^{\mathrm{E}}$, $\boldsymbol{Q}^{\mathrm{I}}$ and $\boldsymbol{Q}^{\mathrm{F}}$ result from electrical flow, plastic deformation and friction, respectively. Besides, coupling problems may also be caused by temperature-dependent electrical rates $\boldsymbol{K}^{\mathrm{E}}$ and mechanical stiffness $\boldsymbol{K}^{\mathrm{M}}$. In thermal analysis, coupling problems can also arise from convection, radiation, temperature-dependent thermal conductivity, and specific heat capacity.

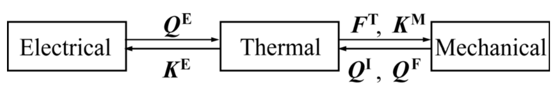


**Fig. 3** Schematic drawing of electrical−thermal−mechanical coupling method

In the solving process of macro−micro scale issue, not only the deformation in macro-scale, but also the microstructural evolution mechanisms in micro-scale including DRX and grain growth, are relative to the three basic parameters, i.e. strain, strain rate and temperature. Here, a Johnson−

Mehl−Avrami−Kolmogorov (JMAK) numerical model (Eq. (2)) [19,20] is introduced to express the DRX volume fraction kinetics. In the solving process of macro−micro scale issue by finite element method (FEM), the nodal parameters including strain, strain rate and temperature at every deformation increment are inputted into the DRX kinetic equation to achieve the instant DRX volume fraction [18].

$$\begin{cases} X_{\mathrm{DRX}}=1-\exp\left[-\beta_d\left(\dfrac{\varepsilon-\varepsilon_{\mathrm{c}}}{\varepsilon_{0.5}}\right)^{k_d}\right] \\ \varepsilon_{\mathrm{c}}=a_1\varepsilon_{\mathrm{p}} \\ \varepsilon_{\mathrm{p}}=a_2\dot{\varepsilon}^{m_1}\exp\left(\dfrac{Q_1}{RT}\right) \\ \varepsilon_{0.5}=a_3\dot{\varepsilon}^{m_2}\exp\left(\dfrac{Q_2}{RT}\right) \end{cases} \tag{2}$$

where $\varepsilon_{\mathrm{c}}$ is the critical strain; $\varepsilon_{\mathrm{p}}$ is the peak strain; $\varepsilon_{0.5}$ is the strain of the dynamic recrystallization (DRX) volume fraction reaching 50%; $\beta_d$ and $k_d$ are the material constants; $Q_1$ and $Q_2$ are the deformation activation energy under different conditions, as for Ni80A superalloy, here, $Q_1$=33332.13 J/mol, $Q_2$=47009.41 J/mol; $X_{\mathrm{DRX}}$ is volume fraction of DRX; $a_1$, $a_2$, $a_3$, $m_1$ and $m_2$ are material constants, as for Ni80A superalloy, here, $a_1$=0.403, $a_2$=0.012415, $a_3$=0.0061, $m_1$=0.248 and $m_2$=0.053.

Since the volume fraction of DRX has been calculated from the above equations, the acquisition of DRX grain size is the following job. Here, a Sellars-type model (Eq. (3)) [21] is applied in expressing DRX grain size when the volume fraction of DRX is below 95% and strain is above critical strain. In this equation, DRX grain size is determined by initial grain size, strain rate and deformation temperature.

$$d_{\mathrm{drx}}=ad_0^h\varepsilon^n\dot{\varepsilon}^m\exp\left(\frac{Q}{RT}\right) \tag{3}$$

where $d_{\mathrm{drx}}$ is the grain size of DRX; $d_0$ is the initial grain size, $a$, $h$, $n$ and $m$ are material constants, here, $a$=0.00025, $h$=1, $n$=−0.39, $m$=−0.07; $Q$ is the deformation activation energy, and its value here is 80505.1 J/mol.

In addition, another Sellars-type model as Eq. (4) is used to describe the grain growth kinetics when the volume fraction of the DRX is above 95% [20]. In this equation, the grown grain size is expressed by the function of initial grain size, heating temperature and holding time.

$$d^{m_2}=d_0^{m_2}+a_4t\exp[Q_4/(RT)] \tag{4}$$

where $d$ is the grain size after growth; $a_4$ and $m_2$ are material constants, and here, $a_4$=120028, $m_2$=2; $Q_4$ is the activation energy after growth, and $Q_4$=92442.75 J/mol; $t$ is the holding time. These important model parameters in the JMAK equations and Sellars-type equations are introduced in details in the literature [22,23]

### 2.2 FEM model of electric upsetting process

In order to uncover the formation mechanism of basin-like depression defect and its influence on the microstructures in an electric upsetting process, a 2D-semi-symmetric finite element model with multi-field and multi-scale coupling was established (see Fig. 4) based on the commercial solver platform MSC. Marc using electrical−thermal−mechanical module. In this model, the billet was set as a plastic object, while the anvil and the clamping electrode were set as rigid objects. Since in a large-scale electric upsetting process, the plastic object is suffered from a severe deformation, the mesh-generator program will regenerate the mesh automatically at any geometrical changes of region elements and will generate mesh on the regions having no mesh. When the boundary of current flow was defined, the left side of anvil and

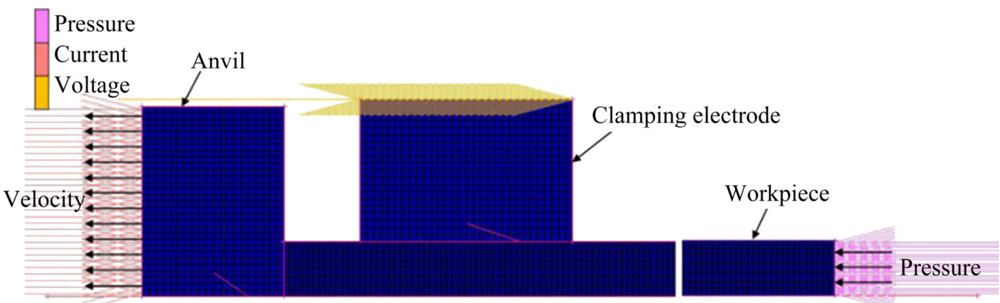


**Fig. 4** Finite element model of electric upsetting process

the upper side of clamping electrode were loaded by high voltage and low voltage, respectively. In addition, the heat transfers between the following contact interfaces were taken into a full consideration, such as the heat conduction between anvil and bar billet, the heat conduction between clamping electrode and bar billet, and the heat convection and the heat radiation between all the objects and environment.

As for an electric upsetting process, at the beginning stage, the maximum temperature region always appears at the contact interfaces between anvil and bar billet. With the upsetting process extending, the maximum temperature region transfers from the contact interface to other spots, and the temperature at the contact interface drops to a relatively low level. This fact reveals that the electric-heating effect at the beginning stage is dominated by the contact resistance, while in the following process the contact resistance becomes lower and lower. The evolution of the contact resistance has been described as a function of temperature and contact pressure by Eq. (5) [17]. It can be concluded that the contact resistivity decreases till zero with the increase of temperature and contact pressure.

$$\rho=1/(a_1T+a_2) \tag{5}$$

where $\rho$ is the contact resistance resistivity, $T$ is the heating temperature, and $a_1$ and $a_2$ are the parameters related to the mass of contact surface and initial contact pressure. Here, it is determined that $a_1$ is 0.87, and $a_2$ is 132.

The basic stress−strain data of Ni80A alloy for the finite element solution are shown in Fig. 5. These data come from a series of isothermal compression tests conducted on a Gleebl−3500 simulator, and this work was introduced in details in the literature [24].

As for the long-time electric upsetting process of a large-scale valve, the high-level multi-stage loading mode of force and current parameters is a basic approach to acquire the desired macro-scale deformation and microstructures. However, the multi-stage loading path schemes are endless. The optimized design in the parameter loading-path is a

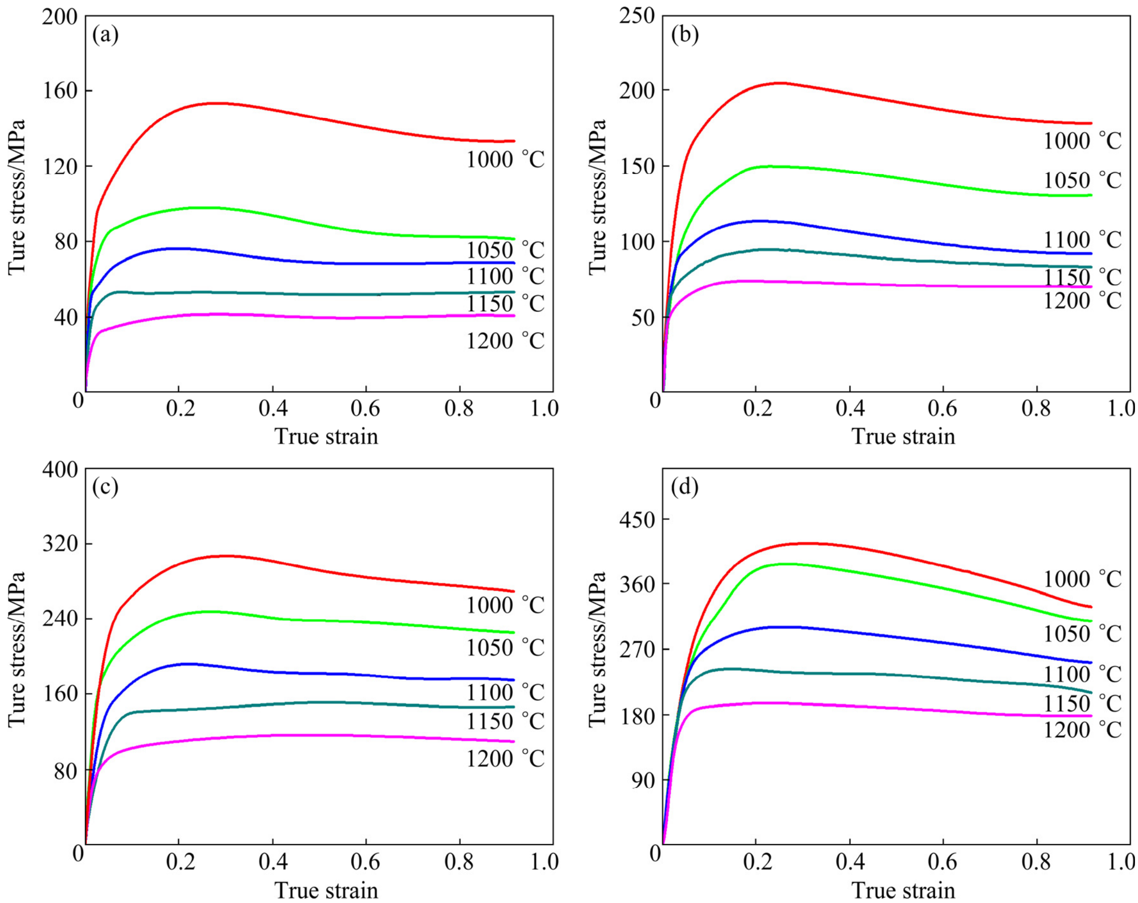


**Fig. 5** True stress−strain curves of Ni80A superalloy at different temperatures and strain rates: (a) 0.01 $s^{-1}$; (b) 0.1 $s^{-1}$; (c) 1 $s^{-1}$; (d) 10 $s^{-1}$ [24]

complex and difficult issue. Furthermore, the design principles should be established. Figure 6 shows one of the most suitable loading-path schemes of force and current parameters for any electric upsetting process, which is concluded from a lot of simulations and experiments. In this scheme, the upsetting stroke is divided into more than 30 sections according to the equipment potential ability. The force parameter and current parameter vary with upsetting stroke. The current loading mode is named as "Single peak" type, while the force loading mode is named as "Flatbed" type. This scheme ensures to achieve a desired shape for component as well as a good grain size control.

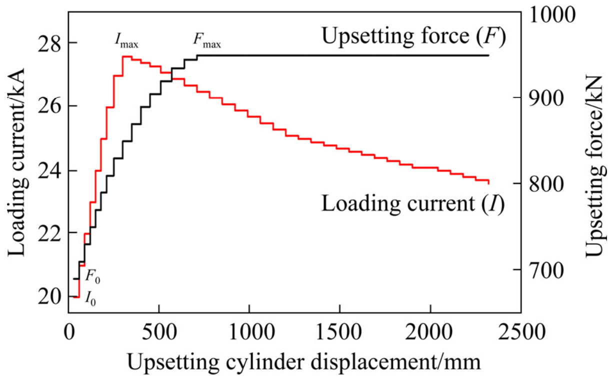


**Fig. 6** Basic scheme for electric upsetting process

The loading path scheme in Fig. 6 is regarded as the basic loading mode for the subsequent investigation. Since the basin-like depression originates in the early stage of electric upsetting process corresponding to the rising stage of current and force parameters, it is essential to study the influence of the parameter changes on the defect during this stage. Therefore in the following discussion of the forming mechanism of the basin-like depression, the basic loading path scheme with the characteristics including initial value, peak value and value level, were scheduled, and then their influences on the defect formation were analyzed and uncovered.

## 3 Numerical results and discussion

### 3.1 Formation of basin-like depression in electric upsetting process

In order to describe the forming process of basin-like depression, the simulation related to the basic loading path scheme was conducted by FEM. The results in Fig. 7 show the evolution process of this defect in the basic loading mode, from which it can be seen that the direction and velocity of material flow in different regions of the deformed material vary with the upsetting process extending. In summary, the forming process of basin-like depression is divided into three deformation stages. It is noted that the three deformation stages occur in the rising stage of current and force parameters as shown in Fig. 6. In order to summarize the change of material flow, in Fig. 7(a), two typical tracks as reference line for defect-existing domain were marked on the FEM model, and then the track variations were simulated. Track 1# is at the leftmost of the "garlic" portion, and Track 2# is in its middle. After a simulation, the positions of element nodes on the two tracks were counted as Figs. 8 and 9. It is illustrated that the flow rate of the outer material is faster than that of the inner material. At the initial stage of basin-like depression, the origination of difference in material flow mainly attributes to two factors. The first is the change of heating rate induced by the transformation of predominant resistance in heating from contact-resistance to material-resistance. The second is the timely different distribution of pressurization speed induced by the step change of hydraulic force along with the force loading path. To sum up, the main reasons for the difference in material flow velocity

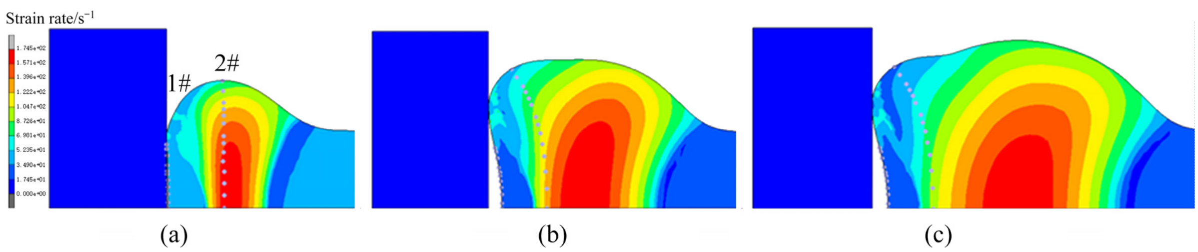


**Fig. 7** Formation process of basin-like depression and distribution of strain rate field: (a) Initial stage of basin-like depression (500 s); (b) Intermediate stage of basin-like depression (750 s); (c) Stabilization stage of basin-like depression (1000 s)

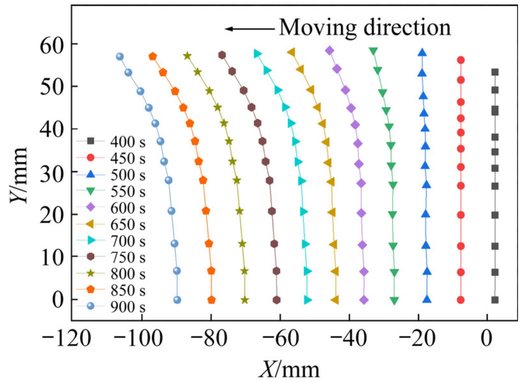


**Fig. 8** Shape variation of Track 1# at diverse time

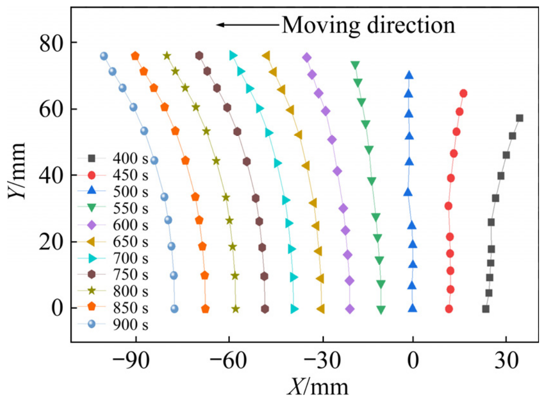


**Fig. 9** Shape variation of Track 2# at diverse time

can be concluded as the comprehensive effect of heating speed and pressurization speed. Such difference in material flow makes the basin-like depression gradually appear. In addition, from Figs. 8 and 9 it can be seen that before the defect shape no longer changes, the flow velocities of the outer material and the inner material are increasingly different. Due to such a difference in flow velocities, the outer material keeps continuously piling up, whereas the inner material is hard to deform. Under the action of uneven material flow velocity, the basin-like depression appearing on contact surface becomes much more apparent. At the stabilization stage of basin-like depression, the deformation near the basin-like depression tends to be stable, which indicates that the defect depth doesn't change along with upsetting process extending.

The change of heating rate can be illustrated by the uneven temperature distribution. Figure 10 shows the temperature field distribution in the formation process of basin-like depression, from which it can be seen that along with the defect transformation from the initial stage to the stabilization stage, the maximum temperature region transfers from the contact interface to the neck of "garlic" portion. In addition, it can be found that the temperature in inner region is higher than that in outer region. It is sure that the portion with higher temperature has better plasticity, so its material flow is better. Consequently, the change of heating rate results in the uneven temperature distribution and then different flow velocities of the inner and outer layers.

### 3.2 Influence of current on basin-like depression formation and mixed grain structure

Since the basin-like depression originates in the rising stage of current, it is of great significance to analyze the influence of rising current on basin-like depression formation. Thus, based on the characteristic of basic loading path pattern considering force as a constant, the current-loading schemes with different levels, peak values and initial values were designed, and their influences on basin-like depression formation and mixed grain structure were simulated and uncovered.

#### 3.2.1 Influence of current level

The current loading paths were scheduled as $0.6I$, $0.8I$, $1.0I$ and $1.2I$, respectively, and the detailed loading paths of different current levels were exhibited in Fig. 11. As illustrated in Fig. 2, the distance between the lowest point of basin-like depression and the anvil surface is employed to evaluate the size of this defect. For different current loading levels, simulation results for the distribution of temperature field, DRX volume fraction field

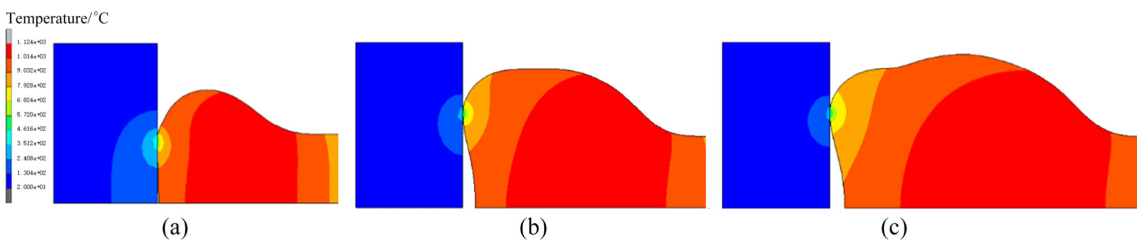


**Fig. 10** Formation process of basin-like depression and distribution of temperature field: (a) Initial stage of basin-like depression; (b) Intermediate stage of basin-like depression; (c) Stabilization stage of basin-like depression

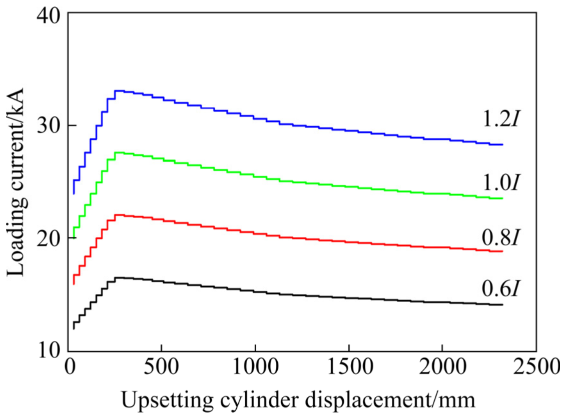


**Fig. 11** Parameter settings under different current levels

and grain size field were derived and shown in Fig. 12. In order to thoroughly clarify the variations of basin-like depression at these current loading levels, the depths of basin-like depression varying with upsetting time were counted, as shown in Fig. 13. It can be seen that the defect depth is enlarged with the increase of current level. The main reason for this can be attributed to two aspects. In Fig. 12(a), at the initial deformation stage, the billet with lower temperature deformed difficultly, especially for the material contacted with the anvil. Thus, the defect depth is relatively low at lower current level. In addition, it is also noted that a significant difference of temperature between inner and outer materials exists. With current level increasing, such a difference will be intensified resulting from the faster material flow at higher current level. With that, the basin-like depression becomes more and more serious with the current level increasing. It is worth emphasizing that the defect depth will reach a stable state as the deformation continues.

In order to intuitively analyze the influence of current level on mixed grain structure, the distribution of mixed grain at diverse current levels was analyzed. It is obviously found in Fig. 12(c) that the mixed grain domain decreases with increasing current level for a fixed force, which indicates that more DRX grains occurred. Comparing Fig. 12(a) with Fig. 12(b), it can be seen that the deformation temperature benefits the occurrence of DRX. This is because more activated

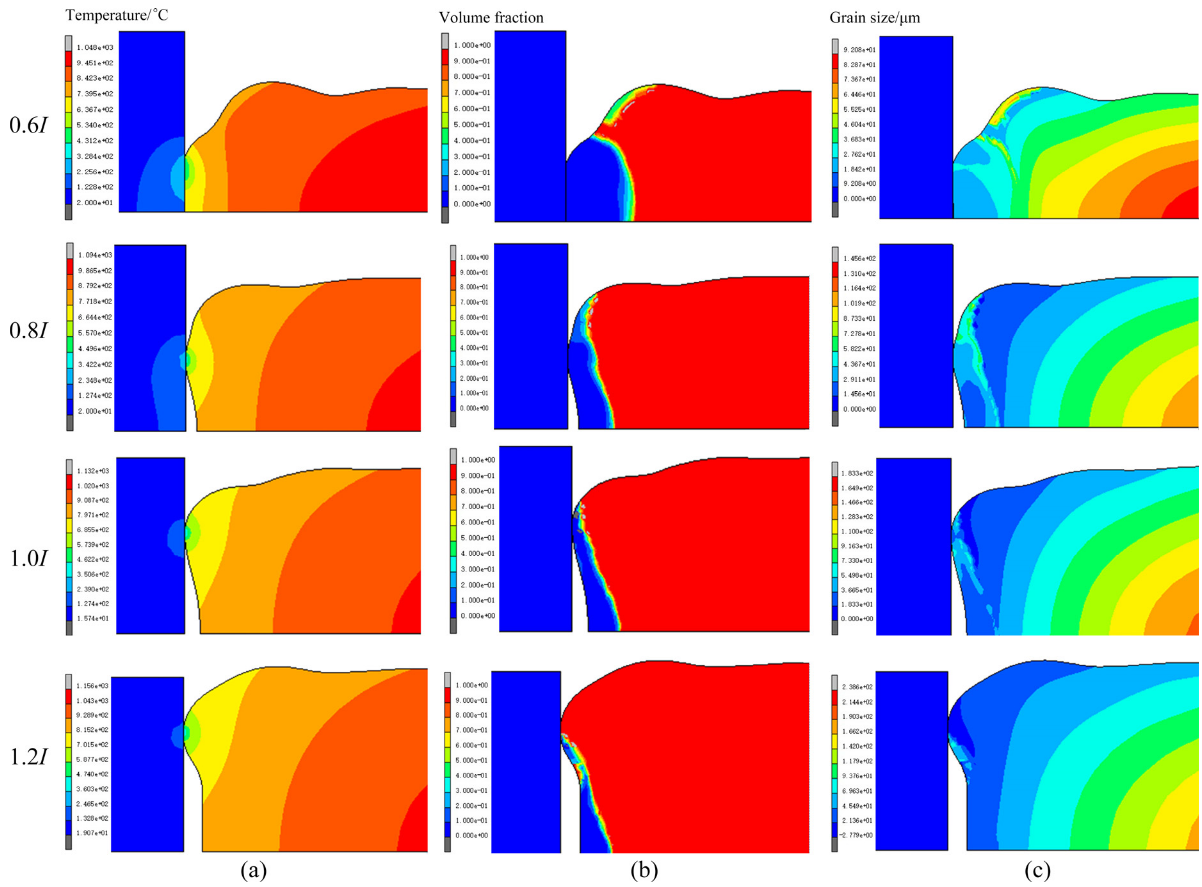


**Fig. 12** Distribution of temperature field (a), DRX volume fraction field (b), and grain size field (c) under different current loading levels

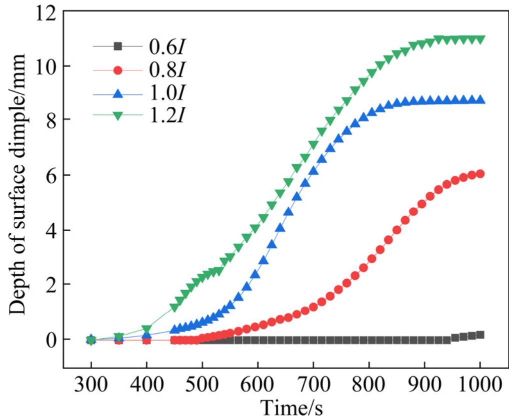


**Fig. 13** Variation of defect depth with time under different current levels

slipping systems and higher grain boundary mobility induced by elevated temperature can significantly enhance the DRX process [6]. However, the average grain size increases with increasing current level. It attributes to the fact that DRX occurs completely and the formed DRX grains will grow at elevated temperatures. So, the difference of average grain size in mixed grain domain decreases at higher current levels.

3.2.2 Influence of initial current

Figure 14 demonstrates the loading paths of different initial current values. The variation of defect depth with time and the distribution of grain size field under different initial currents are shown in Fig. 15. In Fig. 15(a), it is found that the basin-like depression depth increases with the increase of initial current. It is sure that the billet generates more heat at higher initial current and possesses better material flow, which will enhance the basin-like depression.

As for the mixed grain domain exhibited in Fig. 15(b), the area of this domain varies slightly

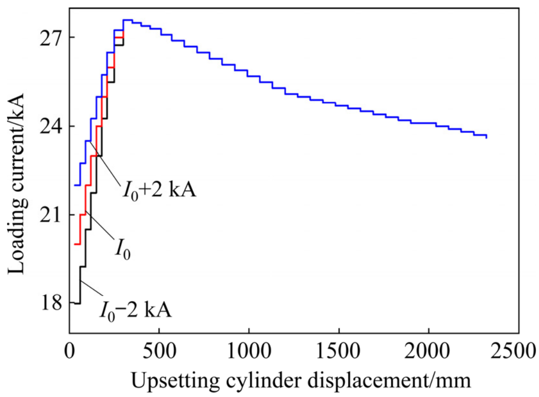


**Fig. 14** Parameter settings under different initial currents

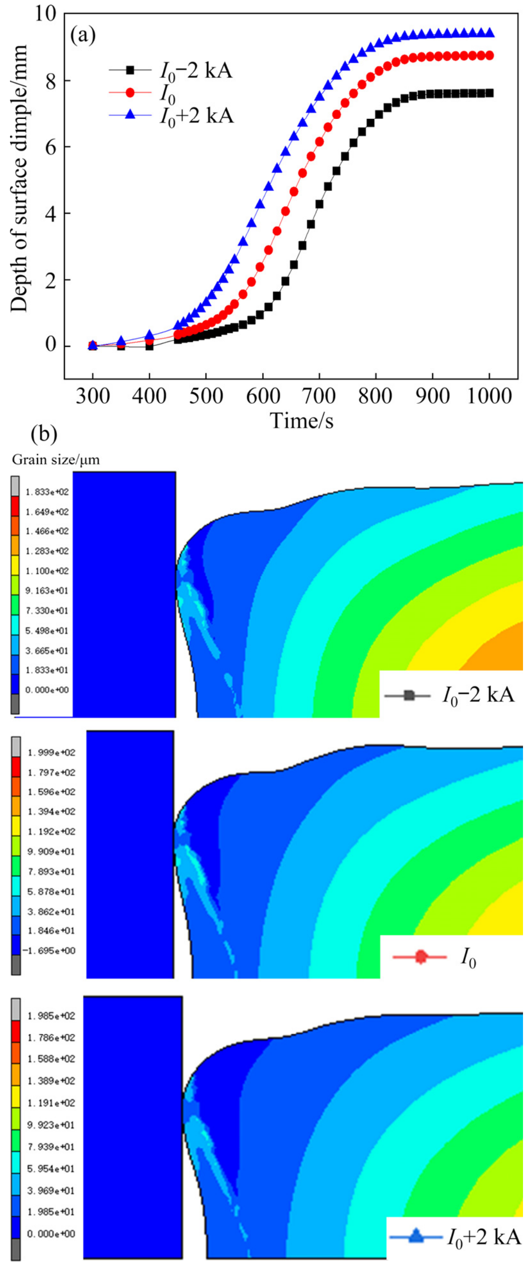


**Fig. 15** Variation of defect depth with time (a) and distribution of grain size field (b) under different initial currents

with initial current increasing. This phenomenon can be attributed to two factors. On the one hand, it is evident that the temperature of billet under higher initial current rises more rapidly than that under lower initial currents. This can also accelerate the occurrence of DRX at the elevated temperature to a large extent. On the other hand, the inputted maximum current of the loading paths is the same, which limits the highest temperature occurring in upsetting process. Consequently, there is no significant difference on the area of mixed grain domain at the loading paths of different initial currents.

3.2.3 Influence of peak current

The loading paths under different peak current values were exhibited in Fig. 16. The defect depths varying with time are shown in Fig. 17(a), and the distribution of grain size field under different peak current values is shown in Fig. 17(b). In Fig. 17(a), at the early forming stage of basin-like depression, since the difference in the inputted current is relatively small, the generated defect depth is almost the same. As upsetting time continues, the loading path with higher peak current value possesses more heat and faster material flow velocity, which led to an obvious difference in the defect depths of these loading paths. As shown in Fig. 17(b), it is apparently found that the mixed grain domain decreases with increase of peak current value. This is mainly because higher temperature can significantly facilitate the DRX grain growth. Thus, the average grain size increases at higher current peak, while the difference of average grain size in mixed grain domain decreases.

Based on the above analysis, it can be concluded that the loading path of current with different initial values, peak values and value levels has strong influence on the formation of basin-like depression and mixed grain structure domain.

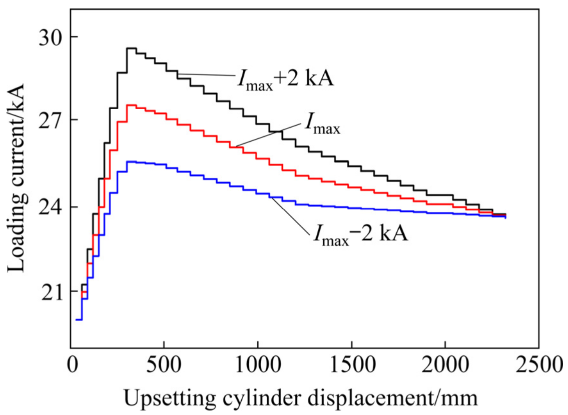


**Fig. 16** Parameter settings under different peak current values

## 3.3 Influence of force on basin-like depression formation and mixed grain structure

Similarly, keeping current as a constant, the force with different levels, peak values and initial values were also designed, and their influences on the basin-like depression formation and mixed grain structure were simulated and uncovered.

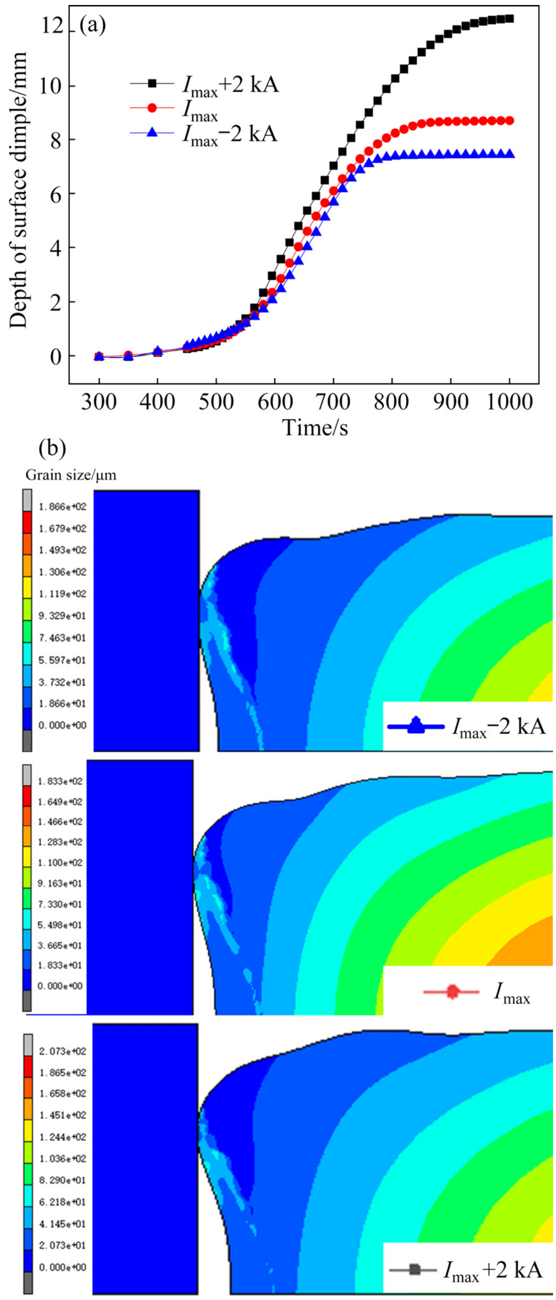


**Fig. 17** Variation of defect depth with time (a) and distributions of grain size field (b) under different peak current values

3.3.1 Influence of force level

The loading paths of force with different levels of 0.6$F$, 0.8$F$, 1.0$F$ and 1.2$F$ were shown in Fig. 18. Figures 19(a−c) show the simulation results for the distributions of temperature field, DRX volume fraction field and grain size field, respectively, and the variations of basin-like depression varying with upsetting time at these loading paths are demonstrated in Fig. 20. It is obviously found that as upsetting time continues,

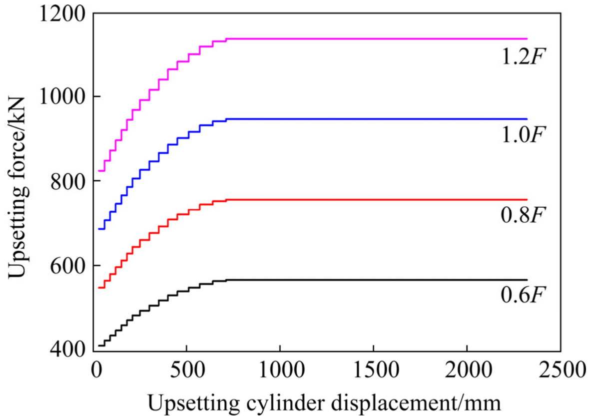


**Fig. 18** Parameter settings under different force levels

the defect depth increases gradually and then keeps a constant in the studied loading paths. Additionally, it can also be noted that the defect depth increases with the increase of force level, while the defect depth at the force level of 1.2$F$ is lower in comparison to the force level of $F$. That is to say, there is a nonlinear relationship between the defect depth and force level. This can be explained as follows: when the force keeps a relatively low level with less than $F$, with force level increasing, the material flow velocity increases, and then the defect depth increases. However, for the same inputted current and higher force level, the billet with a larger upsetting radius possesses a smaller current density on its section, and the rise of temperature is limited. Meanwhile, the forming of basin-like depression is also impeded at lower material flow velocity.

In order to intuitively analyze the influence of force level on mixed grain structure, the distributions of mixed grain at various force levels were analyzed. In Fig. 19(c), it can be observed that the mixed grain domain becomes larger as force level increases. Combining Fig. 19(c) with Fig. 19(b), it is found that with the increase of force level, DRX occurs extremely incompletely in the mixed grain domain. According to Fig. 19(a), by comparing the temperature difference between the outer and inner layers of material at these loading paths, it is noted that the conspicuous temperature difference exists at higher force level, and higher force level can result in lower temperature. So, the mixed grain domain expands with the increase of force level.

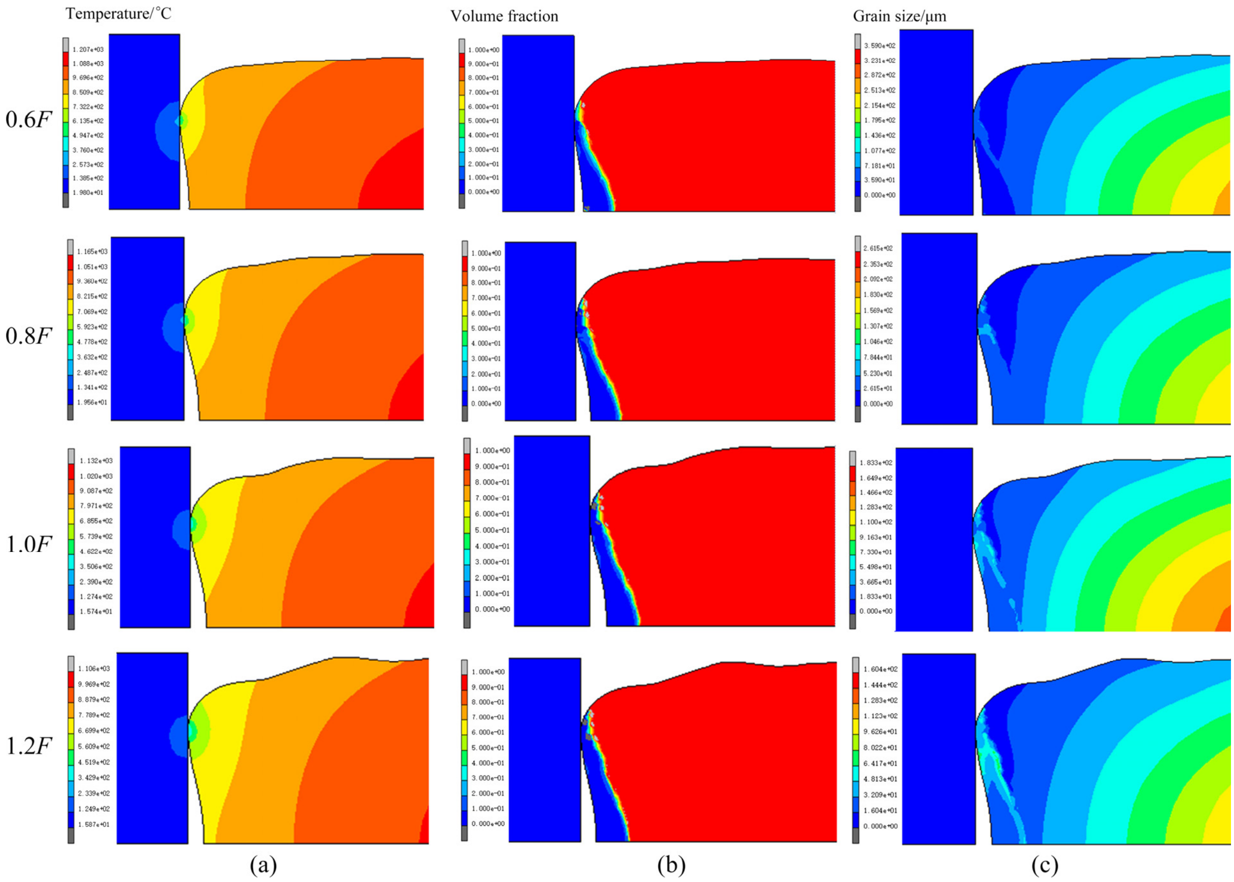


**Fig. 19** Distributions of temperature field (a), DRX volume fraction field (b), and grain size field (c) under different force loading levels

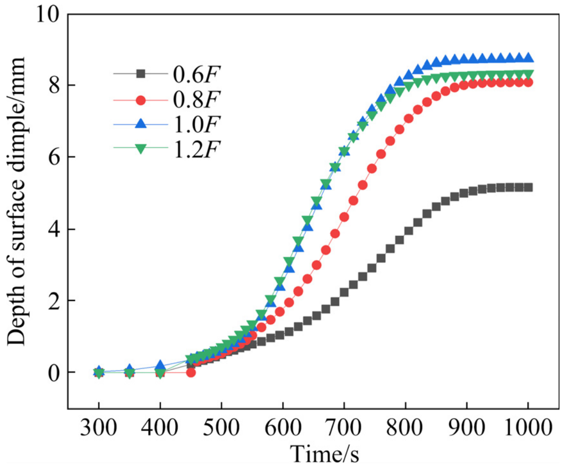


**Fig. 20** Variation of defect depths with time under different force levels

3.3.2 Influence of initial force

The loading paths of different initial force values were exhibited in Fig. 21. Figure 22(a) shows the variation of defect depth with time, and Fig. 22(b) shows the distributions of grain size field under different initial forces. It is found in Fig. 22(a) that the increase of initial force value is beneficial to the reduction of defects. From Fig. 22(a), it is apparent that the rising slopes of the loading paths are different, and lower initial force corresponds to higher pressurization speed. Besides, there is a significant difference in the flow velocity between the outer and the inner layers of material under higher pressurization speed, thus the defect depths will be enhanced with the decrease of the initial force.

As illustrated in Fig. 22(b), the mixed grain domain increases slightly with the initial force increasing. On the one hand, billet deformed under a lower initial force possesses a larger current density on its section, resulting in higher temperature. To some extent, occurrence of DRX is accelerated induced by the elevated temperature. On the other hand, the lower initial force can result in lower strain, which will impede the formation of mixed grain structure. Therefore, the difference of mixed grain domains at the loading paths is not obvious.

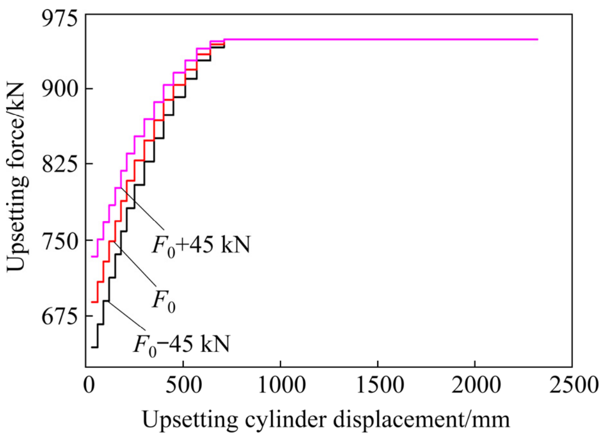


**Fig. 21** Parameter settings under different initial forces

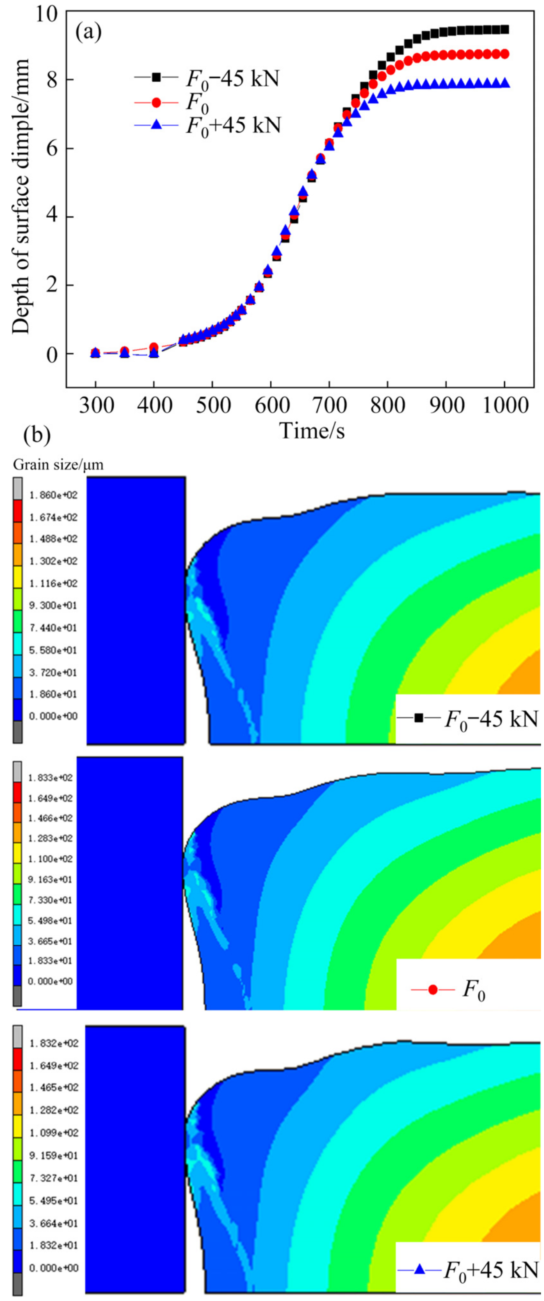


**Fig. 22** Variation of defect depth with time (a) and distribution of grain size field (b) under different initial forces

3.3.3 Influence of peak force

Figure 23 illustrates the loading paths of different force peak values. The variation of defect depth along with time and the distribution of grain size field under different peak force values are shown in Fig. 24. It is observed from Fig. 24(a) that the depth of basin-like depression increases with peak force increasing. This is because higher force strengthens the difference of material flow velocity. As for mixed grain structure, it can be seen from Fig. 24(b) that the mixed grain domain does not vary obviously at different peak forces. The reason for this is similar with the inducing mechanism of the mixed grain domain at different initial forces. With the increase of peak force, the mixed grain domain shows no significant difference owing to the comprehensive action of lower temperature and higher strain.

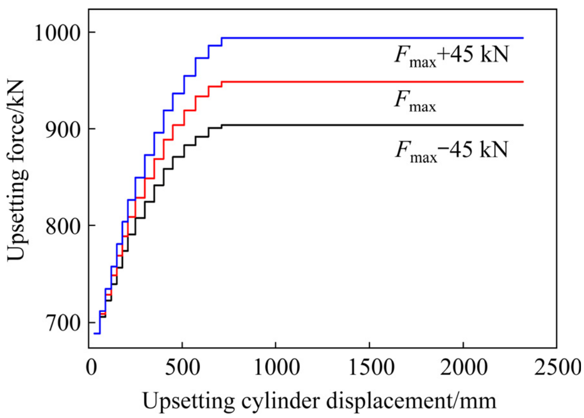


**Fig. 23** Parameter settings under different peak forces

Based on the above analysis, it can be summarized that the formation of basin-like depression and mixed grain domain are strongly influenced by the loading paths of force involving different initial values, peak values and value levels.

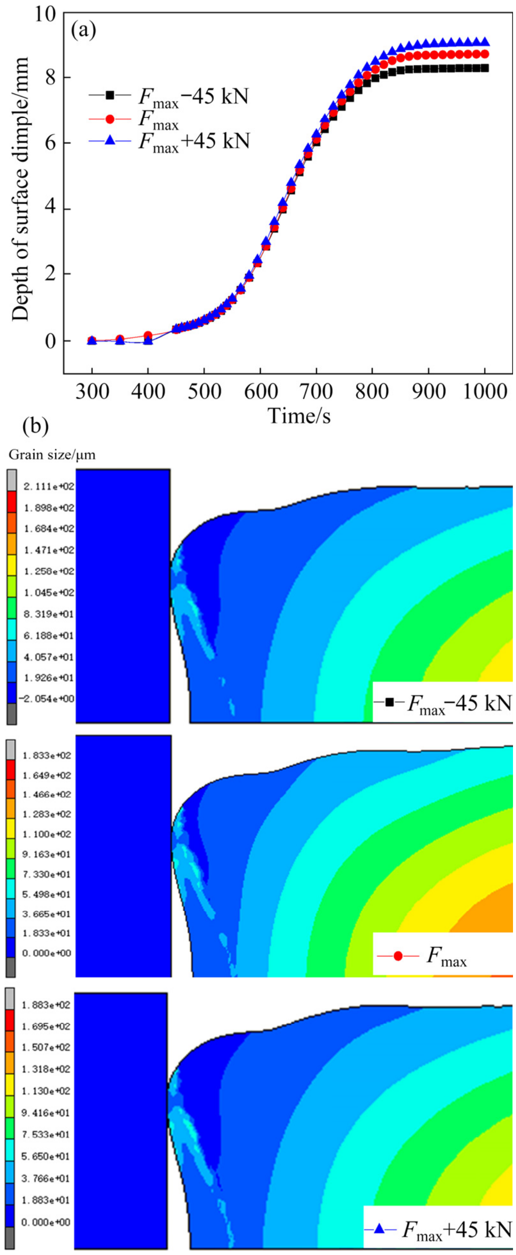


**Fig. 24** Variation of defect depth with time (a) and distribution of grain size field (b) under different peak force values

## 4 Validation of simulation

The physical experiment for the electric upsetting process of Ni80A superalloy, was carried out using basic scheme with multi-stage loading modes of force and current parameters, and the reliability of the developed finite element model was validated. Figure 25(a) shows the experimental results of surface instability and basin-like depression. The defect depth in experiment was measured as 9.15 mm, while the simulation result corresponds to 8.75 mm. The relative error between experiment and simulation results is not greater than 5%, which indicates the correctness and reliability of the finite element model. In addition, the microstructure of one corner of the basin-like depression which was marked in red box of Fig. 25(b) was observed by optical microscopy, as exhibited in Fig. 25(c). The maximum grain size is 210.4 μm and the grain size in nearby region is 40.5 μm. It is noted from Fig. 25(b) that a significant difference can be characterized on the grain size between coarse and fine grains, representing as mixed grain structure. Such microstructures also prove the reliability of the developed finite element model.

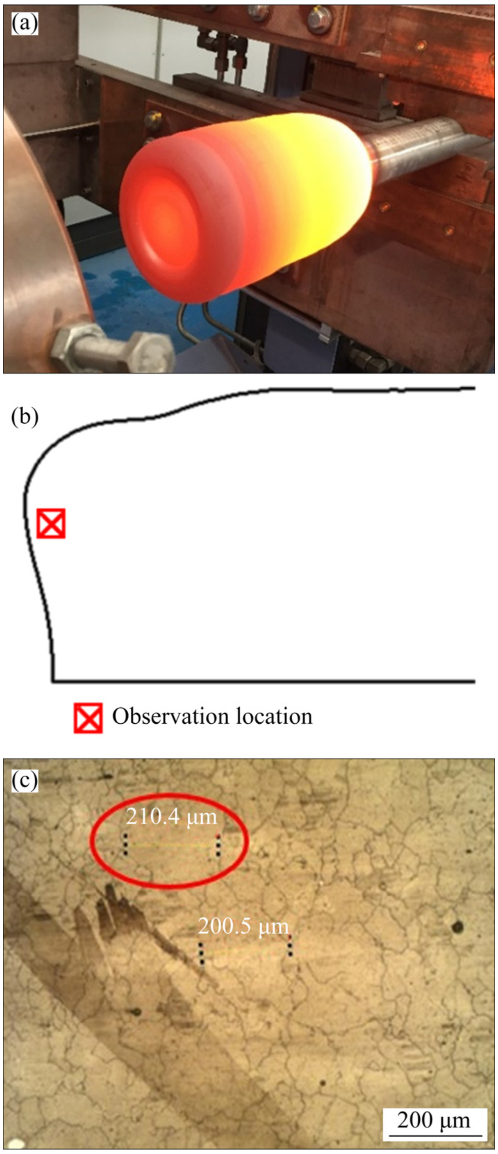


**Fig. 25** Experiment results: (a) Forming shape; (b) Observation location; (c) Microstructure

## 5 Conclusions

(1) In the electric upsetting process of Ni80A superalloy, the deformation instability results in the basin-like depression companied by the mixed grain structure. The main factors that affect the defect are the different flow velocities between outer and inner layers at head deformed portion induced by the changes of heating speed and pressurization speed.

(2) With the decrease of initial current, peak current and current level, the depth of basin-like depression decreases, while the mixed grain domain expands gradually. Moreover, the depth of basin-like depression increases with increase of peak force and force level and decrease of initial force, while the mixed grain domain increases with increase of initial force, peak force and force level.

(3) Simulation results suggest that the defect with smaller basin-like depression and mixed grain domain needs to coordinate the parameter matching of force and current.

(4) The correctness and reliability of the established finite element model were conducted by the physical experiment for the electric upsetting process. The relative error of the depth of basin-like depression between simulation and experiment results is limited within 5%.

## Acknowledgments

The authors are grateful for the support from the National Natural Science Foundation of China (No. 52175287), and Open Fund of State Key Laboratory of Materials Processing and Die & Mould Technology, China (No. P2020-001).

## References

[1] KOMMEL L. Microstructure and properties characterization of polycrystalline Ni−Fe−Cr-based superalloy EP-718E after electric upsetting [J]. Key Engineering Materials, 2016, 721: 467−472.

[2] YANAGIMOTO J, IZUMI R. Continuous electric resistance heating−Hot forming system for high-alloy metals with poor workability [J]. Journal of Materials Processing Technology, 2009, 209: 3060−3068.

[3] DAMODARAM R, RAMAN S G S, RAO K P. Microstructure and mechanical properties of friction welded alloy 718 [J]. Materials Science and Engineering A, 2013, 560: 781−786.

[4] NEUGEBAUER R, ALTAN T, GEIGER M, KLEINER M, STERZING A. Sheet metal forming at elevated temperatures [J]. CIRP Annals, 2006, 55: 793−816.

[5] BARIANI P F, BRUSCHI S, GHIOTTI A, TURETTA A. Testing formability in the hot stamping of HSS [J]. CIRP Annals, 2008, 57: 265−268.

[6] QUAN Guo-zheng, ZHANG Yu-qing, ZHANG Pu, MA Yao-yao, SHI Rui-ju. Correspondence between low-energy twin boundary density and thermal-plastic deformation parameters in nickel-based superalloy [J]. Transactions of Nonferrous Metals Society of China, 2021, 31: 438−455.

[7] BEER A G, BARNETT M R. Microstructure evolution in hot worked and annealed magnesium alloy AZ31 [J]. Materials Science and Engineering A, 2008, 485(1/2): 318−324.

[8] SHAHZAD M, WAQAS H, RAFI-UD-DIN, QURESHI A H, WAGNER L. The roles of Zn distribution and eutectic particles on microstructure development during extrusion and anisotropic mechanical properties in a Mg−Zn−Zr alloy [J]. Materials Science and Engineering A, 2015, 620: 50−57.

[9] SHAHZAD M, QURESHI A H, WAQAS H, RAFI-UD-DIN. Influence of pre- and post-extrusion heat treatments on microstructure and anisotropy of mechanical properties in a Mg−Al−Zn alloy [J]. Materials & Design, 2013, 51: 870−875.

[10] WANG Xin, HUANG Zai-wang, CAI Biao, ZHOU Ning, MAGDYSYUK O, GAO Yan-fei, SRIVATSA S, TAN Li-ming, JIANG Liang. Formation mechanism of abnormally large grains in a polycrystalline nickel-based superalloy during heat treatment processing [J]. Acta Materialia, 2019, 168: 287−298.

[11] NUASRI P, AUE-U-LAN Y. Influence of process parameters on electric upsetting process by using finite element modeling [J]. Key Engineering Materials, 2017, 728: 42−47.

[12] JEONG H S, CHO J R, LEE N K, PARK H C. Simulation of electric upsetting and forging process for large marine diesel engine exhaust valves [J]. Materials Science Forum, 2006, 510/511: 142−145.

[13] ELAIYARAJA K, PERIYASAMY P. Inprocess quality control through proportionate valve in electrical upsetting of engine valves [J]. Applied Mechanics and Materials, 2014, 592/593/594: 2665−2670.

[14] SUN Y, LIU T, ZHANG Z, ZHANG T, LUO T. Optimum control of process parameters in electrical upsetting [J]. Journal of Engineering Manufacture, 2003, 217:1259−1263.

[15] QUAN Guo-zheng, ZOU Zhen-yv, ZHANG Zhi-hua, PAN Jia. A study on formation process of secondary upsetting defect in electric upsetting and optimization of processing parameters based on multi-field coupling FEM [J]. Materials Research, 2016, 19: 856−864.

[16] NUASRI P, AUE-U-LAN Y. Investigation of the “surface dimple” defect occurring during the production of an electric upsetting process by viscoplastic finite element modeling [J]. The International Journal of Advanced Manufacturing Technology, 2018, 98(1/2/3/4): 1047−1057.

[17] QUAN Guo-zheng, ZHANG Le, AN Chao, ZOU Zhen-yu. Multi-variable and bi-objective optimization of electric upsetting process for grain refinement and its uniform distribution [J]. International Journal of Precision Engineering and Manufacturing, 2018, 19: 859−872.

[18] QUAN Guo-zheng, LUO Gui-chang, WEN H R. Influence of electric upsetting process variables on temperature field evolution by multi-field coupling finite element analysis [J]. International Journal of Precision Engineering and Manufacturing, 2015, 16(7): 1525−1531.

[19] JI Guo-liang, LI Fu-guo, LI Qing-hua, LI Hui-qu, LI Zhi. Research on the dynamic recrystallization kinetics of Aermet100 steel [J] Materials Science and Engineering A, 2010, 527: 2350−2355.

[20] CHEN Ming-song, LIN Y C, MA Xong-song. The kinetics of dynamic recrystallization of 42CrMo steel [J]. Materials Science and Engineering A, 2012, 556: 260−266.

[21] QUAN Guo-zheng, LUO Gui-chang, LIANG Jian-ting, WU Dong-sen, MAO An, LIU Qiao. Modelling for the dynamic recrystallization evolution of Ti−6Al−4V alloy in two-phase temperature range and a wide strain rate range [J]. Computational Materials Science, 2015, 97: 136−147.

[22] QUAN Guo-zheng, LI Yong-le, ZHANG Le, WANG Xuan. Evolution of grain refinement degree induced by dynamic recrystallization for Nimonic 80A during hot compression process and its FEM analysis [J]. Vacuum, 2017, 139: 51−63.

[23] QUAN Guo-zheng, ZHANG Pu, MA Yao-yao, ZHANG Yv-qing, LU Chao-long, WANG Wei-yong. Characterization of grain growth behaviors by BP-ANN and Sellars models for nickle-base superalloy and their comparisons [J]. Transactions of Nonferrous Metals Society of China, 2020, 30: 2435−2448.

[24] QUAN Guo-zheng, PAN Jia, WANG Xuan, ZHANG Le. Correspondence between grain refinements and flow softening behaviors at Nimonic 80A superalloy under different strain rates, temperatures and strains [J]. Materials Science and Engineering A, 2017, 679: 358−371.


# Ni80A 高温合金电镦成形中盆状凹陷的形成机理


权国政[1,2,3]，盛 雪[1]，杨 焜[1]，余炎泽[1]，熊 威[4]

1. 重庆大学 材料科学与工程学院 先进模具智能制造重庆市重点实验室，重庆 400044；

2. 华中科技大学 材料成形与模具技术国家重点实验室，武汉 430074；

3. 南京杰品智能科技股份有限公司，南京 210000；

4. 清华大学 核能与新能源技术研究所 先进核能技术协同创新中心

先进反应堆工程与安全教育部重点实验室，北京 100084



**摘 要**：大规格气阀在电镦成形过程中经常存在盆状凹陷缺陷，并伴随混晶组织，缺陷对工件的显微组织和力学性能影响较大。为了分析盆状凹陷的形成过程，建立 Ni80A 高温合金多场、多尺度耦合的电镦有限元模型。随后，通过改变力、电流参数的初始值、峰值和水平，设计一系列力和电流参数加载路径方案，模拟并揭示参数对盆状凹陷和混晶结构的影响。结果表明，电镦成形过程中加热速度和加压速度的变化导致坯料内外层的流速不同，从而产生盆状凹陷。通过力和电流参数的协调，可以对这些缺陷进行优化。最后，通过电镦工艺的物理实验验证有限元模型的有效性和可靠性。



**关键词**：电镦工艺；缺陷；Ni80A 高温合金；显微组织演化；混晶组织

**(Edited by Xiang-qun LI)**